European Polymer Journal 236 (2025) 114159

Contents lists available at ScienceDirect

European Polymer Journal

journal homepage: www.elsevier.com/locate/europolj

Optimizing the piezoelectric response of poly(vinylidene fluoride-*co*-trifluoroethylene) electrospun mats: effects of copolymer composition, microstructure and thermal treatments

Michele Zanoni [a], Niccolò Braidi [a], Giacomo Selleri [b], Dario Cavallo [c], Maria Letizia Focarete [a,d,e], Davide Fabiani [b,f], Chiara Gualandi [a,d,f,*]

[a] Department of Chemistry "Giacomo Ciamician", University of Bologna, Via Gobetti 85, 40129 Bologna, Italy
[b] Department of Electrical, Electronic, and Information Engineering, University of Bologna, Viale Risorgimento 2, 40136 Bologna, Italy
[c] Department of Chemistry and Industrial Chemistry, University of Genova, Via Dodecaneso 31, 16146 Genova, Italy
[d] INSTM UdR of Bologna, University of Bologna, Via Gobetti 85, 40129 Bologna, Italy
[e] Health Sciences & Technologies (HST) CIRI, University of Bologna, Via Tolara di Sopra 41/E, 40064 Ozzano Emilia Bologna, Italy
[f] Interdepartmental Center for Industrial Research on Advanced Applications in Mechanical Engineering and Materials Technology, CIRI-MAM, University of Bologna, Viale Risorgimento, 2, 40136 Bologna, Italy

ARTICLE INFO

Keywords:
Electrospinning
Piezoelectricity
PVDF-TrFE
Poling
Annealing

ABSTRACT

Electrospun piezoelectric polymers have attracted enormous interest in recent decades due to their flexibility, lightweight, and good piezoelectric response. This work investigates structure–property relationships in a series of electrospun poly(vinylidene fluoride-*co*-trifluoroethylene) (PVDF-TrFE) copolymers to find the conditions to maximize the piezoelectric charge coefficient, d_{33}. Nanofibrous mats of PVDF-TrFE at different molar fraction compositions are annealed and/or poled at their respective Curie Temperatures and then characterized using DSC, WAXD, FT-IR, and piezometry. The data collected for the as-spun, annealed, and/or polarized samples are initially analyzed individually, followed by an evaluation of property interrelations. The results show a positive correlation between the d_{33} and the crystallinity degree and the crystallite size, while a negative correlation with the FT-IR absorbances associated with gauche defects is found. Interestingly, a linear combination of these three properties proves a good predictor of the d_{33} value. Notably, during this investigation, we measured d_{33} as high as 37.1, 42.7 and 34.7 pC N^{-1}, for the 70:30, 75:25, 80:20 molar fractions, respectively, ranking among the highest reported for nanofibrous PVDF-TrFE mats. This outstanding result is obtained thanks to the synergic effect of annealing and poling treatments.

1. Introduction

Flexible and portable electronic devices are actively being investigated for their promising advantages in various applications within the fields of robotics, advanced human healthcare, artificial intelligence, and wearable electronics [1–4]. An essential feature of wearable systems is an autonomous power supply. To this end, various methods have been proposed to exploit mechanical motion as a natural power source [5–7]. For instance, the triboelectric transducing mechanism generates electric charges with opposite signs at the interface between two insulating materials through friction [8,9]. Based on this principle, self-powered sensors and triboelectric nanogenerators (TENGs) have been developed using various materials with distinct charge affinities [10–13]. Alternatively, the piezoelectric effect, which relies on the intrinsic polarization of the material, has been widely investigated for developing piezoelectric nanogenerators (PENGs) [14–16], tactile flexible sensors [1,17,18], self-sensing composite materials for structural health monitoring (SHM) [19], and energy harvesting devices [20–22]. Textiles are ideal for wearable electronics thanks to their flexibility, porosity, breathability, and lightweight [23]. Compared to other fiber fabrication technologies, nowadays electrospinning offers versatile manufacturing and cost-effectiveness for the production of highly porous and lightweight polymeric materials, allowing the use of additives to customize their performances [24]. The electrospinning of poly(vinylidene fluoride) (PVDF) has attracted enormous interest in recent decades. In fact, this technique promotes the preferential formation of the polar β-phase

* Corresponding author at: Department of Chemistry "Giacomo Ciamician", University of Bologna, Via Gobetti 85, 40129 Bologna, Italy.
E-mail address: c.gualandi@unibo.it (C. Gualandi).

https://doi.org/10.1016/j.eurpolymj.2025.114159
Received 21 March 2025; Received in revised form 31 May 2025; Accepted 19 July 2025
Available online 20 July 2025

while the polymer jet elongates during its travel from the needle to the grounded collector [25–28]. For this reason, strong efforts have been made to study the various effects exerted by the electrospinning parameters on the promotion of the ferroelectric β-phase over the paraelectric α-phase, such as polymer solution viscosity, voltage applied to the needle, and degree of alignment of the nanofibers [29–31]. Differently from PVDF, which crystallizes in the thermodynamically favored non-polar α-phase, the copolymers of poly(vinylidene fluoride-*co*-trifluoroethylene) (PVDF-TrFE) preferentially form a polar crystalline phase similar to the β-phase of PVDF, regardless of processing methods. Indeed, it is well-documented that VDF and TrFE monomers cocrystallize [32,33] and the inclusion of TrFE units in the copolymer promotes the preferential formation of the all-trans conformation (β-like phase) over the trans-gauche alternate conformation (α-like phase) by allowing greater rotational freedom of the molecular chains around the chain axis [34,35]. Electrospun PVDF and copolymers of PVDF-TrFE have been thoroughly studied to develop a new generation of piezoelectric devices, including highly sensitive e-skins and tactile sensors. The highly porous nanofibrous membranes have been integrated into various materials, both for flexible applications [23,36] and SHM systems of composite materials [37,38], with minimal impact on the mechanical properties of the structures. Additionally, the energy conversion capabilities of the PVDF-TrFE nanofibers have been utilized to develop wearable energy-harvesting systems [39–41]. One notable advantage of electrospinning is the possibility to obtain piezoactive fibers without requiring additional poling treatment, as the electrical field applied during the process may facilitate the preferential orientation of molecular dipoles [42–44]. However, the degree of residual polarization depends significantly on the specific electrospinning setup [45]. Moreover, the underlying mechanisms driving electromechanical transduction in unpoled electrospun samples remain a topic of debate and are not yet fully understood. In a recent study, it was demonstrated that the electret response is the main cause for the observed strong electromechanical transduction due to the accumulation of triboelectric surface charges and trapped space charge [24]. Despite these promising characteristics, achieving high piezoelectric performance – crucial for applications such as energy harvesting – still requires a poling process. This step enhances the alignment of electrical dipoles in a common direction, thereby achieving greater polarization. Furthermore, for maximizing the electromechanical performance of the material, it has been reported that annealing and poling treatments performed slightly above the Curie Temperature (T_C) reduce the gauche defects in the ferroelectric phase, increasing the degree of crystallinity and the β-phase concentration [46,47]. A recent work has highlighted the importance of gaining detailed and quantitative information, achieved by using solid-state nuclear magnetic resonance spectroscopy, on the local order of PVDF to better understand its macroscopic properties [48]. In this work, we leverage annealing and poling treatments to optimize the electromechanical performance of electrospun PVDF-TrFE copolymers with different molar compositions, without compromising fiber morphology. A systematic investigation was conducted using Differential Scanning Calorimetry (DSC), Wide-Angle X-ray Diffraction (WAXD), and Fourier-Transform Infrared Spectroscopy (FT-IR) to explore correlations among the thermal, spectroscopic, and crystallographic properties of the different samples. The study then examined how these properties relate to the piezoelectric coefficients (d_{33}) of the electrospun mats, which measures the charge displaced by the material under mechanical stress. The goal was to identify the key factors influencing the piezoelectric behaviour of the nanofiber materials and determine the optimal conditions for maximizing d_{33}, while keeping unaltered the fiber morphology.

2. Results and discussion

Nanofibrous mats made up of randomly oriented fibers were prepared from polymeric solutions of PVDF-TrFE copolymers (70:30, 75:25, 80:20 molar fraction of VDF:TrFE). For each molecular composition, the polymers were electrospun to produce as-spun mats (AS), followed by thermal annealing to obtain annealed mats (AN). Poling was then applied to both as-spun (AS-P) and annealed samples (AN-P). As described in the experimental section, both annealing and poling temperatures were set based on the Curie temperature (T_C, the ferroelectric-to-paraelectric phase transition) determined from the second DSC heating scan performed on the pristine copolymers after erasing their thermal history (Fig. S2). The samples were characterized to highlight the influence of both annealing and poling processes on the structure–property correlations with the final aim to determine the main factors affecting the piezoelectric charge coefficient (d_{33}). This assumes that the samples do not exhibit intrinsic morphological differences that could influence their properties. Consequently, we begin by presenting SEM imaging which allows to assess whether the fiber morphology was affected either by sample annealing or poling. SEM images reported in Fig. 1 (*first column*) show no significant morphological differences between the AS and AN samples, confirming that the annealing treatment did not affect the fiber morphology. Conversely, after the poling treatment, the AS fibers collapsed, especially on the side of the sample in contact with the live electrode side (Fig. 1, samples AS-P in the *second column*). We attribute this finding to an electrostatic attractive force established between the mat that, according to previous studies, is expected to retain a negative surface charge after electrospinning [49,50], and the positively charged poling electrode. This electrostatic force has the effect to compact the porous structure, with the fiber layers more far away from the electrode compressing the fiber layer in contact with the electrode. Notably, the annealed samples better preserved their original morphology after poling. This is likely due to increased crystallinity, as we will discuss later, which stiffened the fibers. Regardless of these qualitative differences, the statistical analysis of the distributions of fiber diameter (Fig. 1, *histograms*; data provided in Table S1) indicates no significant differences among the samples. This allows us to rule out morphology as a factor contributing to the differences in properties observed later.

To highlight the effect of annealing and poling on the thermal properties of the electrospun samples we observe the first heating scan of the DSC curves (Fig. 2, data reported in Table S2). All the AS samples (Fig. 2, *blue lines*) exhibit a low-T endotherm in the range 50–70 °C, due to the presence of unstable secondary crystals formed during annealing at RT [51,52]. The second endothermal peak (T_C) occurs at extremely low values in all AS samples, reflecting the low crystal quality achieved during electrospinning. This is likely due to the rapid solidification of the polymers during the electrospinning process, which does not allow sufficient time for high-quality crystal formation, as previously found for other polymers [53,54].

For each composition, the AN, AS-P and AN-P samples (Fig. 2, *green*, *red* and *black lines*, respectively) show an overall increase of T_C and ΔH_C (Table S2), meaning that both annealing and poling have a remarkable effect on polymer microstructure. This was previously attributed to a decrease in the number of gauche defects in the all-trans chains [46]. Specifically, in all copolymers, the T_C increases in both the AN samples and in the poled samples, with the AN-P samples showing the highest values of T_C for each composition, highlighting the synergic effect of thermal annealing and poling in improving the thermal stability of the ferroelectric phase. The values of ΔH_C increased significantly following annealing and/or poling, showing an enhancement ranging from two to four times compared to the as-spun counterpart (Table S2).

Due to cocrystallization of VDF and TrFE monomers in the same crystal lattice, determining the crystallinity degree from DSC analysis is complex, as the effect of comonomer inclusion on the variation in the crystal's heat of fusion is unknown [55–59]. Thus, we determined crystallinity degree (χ_c) and crystallite size (D) by WAXD analysis (Fig. S3). The poling process increases both χ_c and D in AS-P samples for all three copolymers (Fig. 3a, *crosses*). Notably, the 75:25 copolymer exhibits a significantly greater increase in D compared to the other copolymers. Similarly, in AN samples both χ_c and D significantly increase

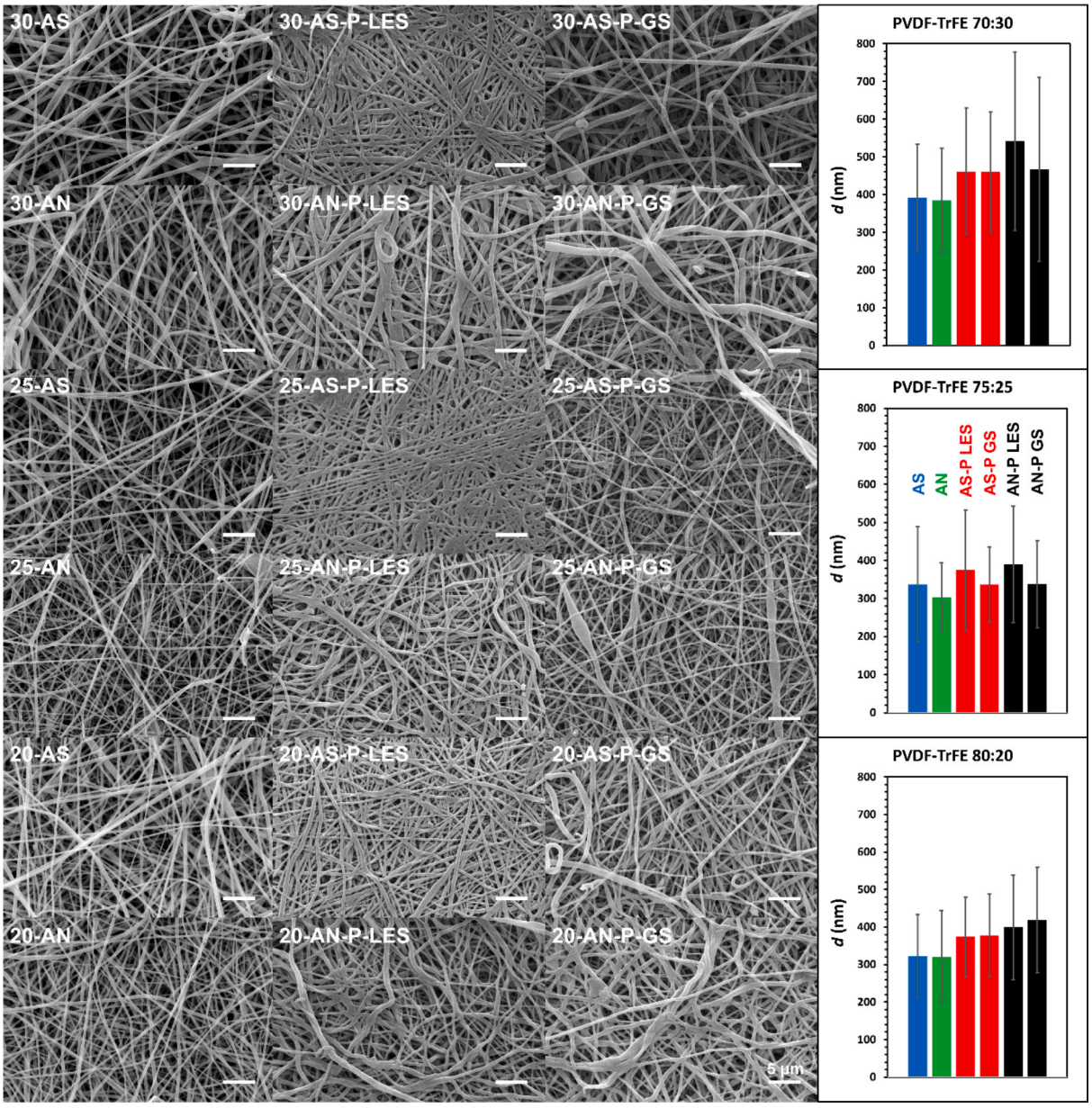

Fig. 1. Representative SEM images of the investigated samples. *First column*: the three as-spun mats of the copolymers (AS, *odd rows*) and the corresponding three annealed mats (AN, *even rows*); *Second column*: the corresponding poled samples observed at the live electrode side; *Third column*: corresponding poled samples observed at the grounded electrode side. For the unpoled samples, only one side is shown as there were no significant differences between the two sides of the same sample. Scale bar = 5 µm. Adjacent to the SEM images, the histograms display the mean diameters (d) of the various samples, categorized by copolymer and treatment. LES = Live Electrode Side; GS = Grounded Side.

with poling (Fig. 3a, *triangles*). Comparing the two treatments, χ_c increases more as a consequence of the annealing than poling, whereas D is enhanced more by poling than annealing. The synergistic effect of annealing and poling is evident in the AN-P samples, which show the highest χ_c and D values (Fig. 3a, *short dash*), with the 75:25 copolymer exhibiting the highest values among the three tested compositions. Furthermore, χ_c and ΔH_C show a significant positive correlation between them for each polymer composition (Fig. 3b). We also observe that the ΔH_C versus χ_c slope increases as the TrFE content decreases, meaning that the TrFE content negatively correlates with the energy required for the ferroelectric to paraelectric phase transition, which involves the free rotation of the $-CF_2-$ units around the chain axis.

Regarding the infrared (FT-IR) analysis, according to the literature, the peaks at 1284 cm^{-1} [59–68], 1083 cm^{-1} [60,65], and 841 cm^{-1} [60,61,63–69] are associated with the β-phase, while the peaks at 974 cm^{-1} [60–66,68], 883 cm^{-1} [63,64,69] 808 cm^{-1} [63,64,66,68], and 760 cm^{-1} [60,63–67], are indicative of the α-phase. Interestingly, there are some references which attribute the 1399 cm^{-1} peak to the β-phase [63,68] and others to the α-phase [61,62], meanwhile Arrigoni et al. concluded that both the α- and β-phase concur to this peak, together with the 883 cm^{-1} one [60]. The peak at 1123 cm^{-1} has been attributed to the TrFE content [60]. FT-IR has also been reported as a technique to identify gauche defects in the β-like phase. This phase is characterized by crystals where all bonds adopt a trans conformation. When this trans sequence is interrupted by a gauche conformation, a gauche defect is said to occur [70]. The presence of these defects reduces the overall dipole moment of an all-trans sequence, consequently decreasing the piezoelectric properties of the material. Literature reports indicate that FT-IR peaks at 906 cm^{-1} and 1238 cm^{-1} are associated with the presence of gauche defects [60]. The aforementioned peaks are highlighted

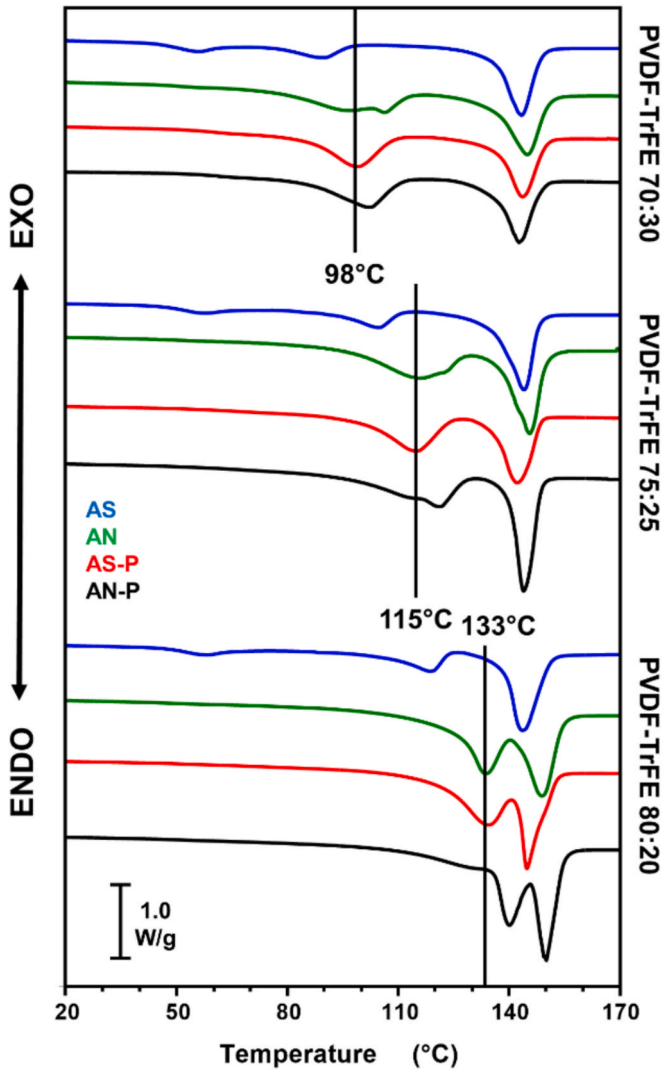

Fig. 2. Overlay of the first heating scans of AS (*blue*), AN (*green*), AS-P (*red*) and AN-P (*black*) samples of the 70:30, 75:25 and 80:20 copolymers. The black vertical lines indicate the temperatures of annealing and poling for each copolymer.

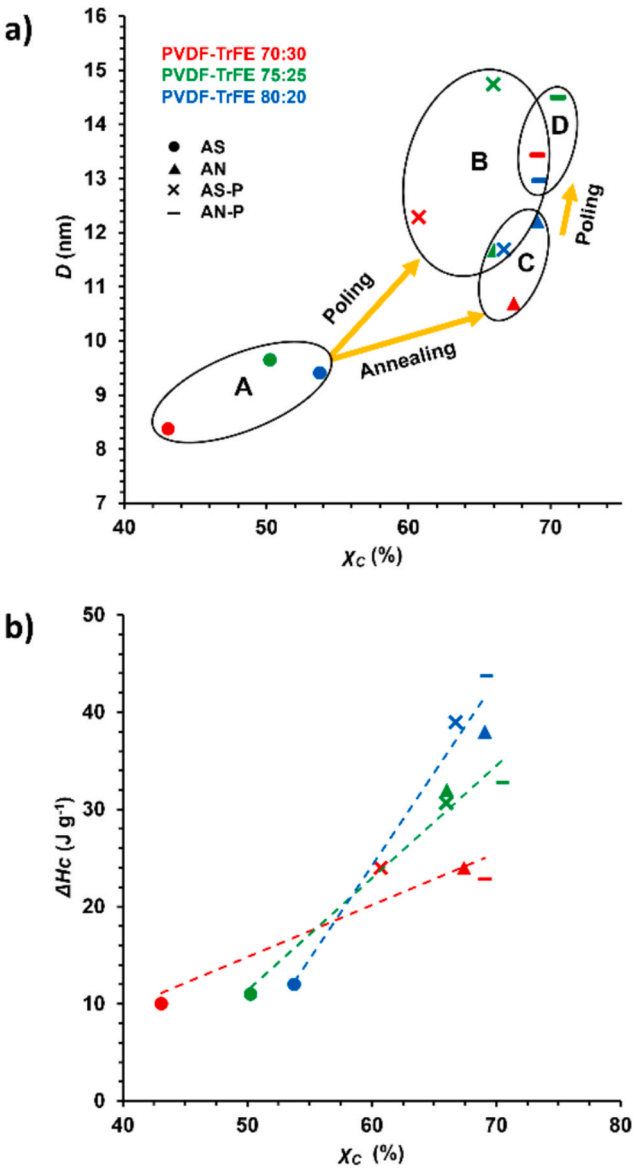

Fig. 3. a) Plot of the crystallite size (D) against the crystallinity degree (χ_c), both were extrapolated from the WAXD diffraction patterns of the samples: AS (*circle*), AN (*triangle*), AS-P (*crosses*), and AN-P (*short dash*). The points are colored *red* for the 70:30 copolymer, *green* for the 75:25 copolymer and *blue* for the 80:20 copolymer. b) Plot of Curie enthalpy (ΔH_C) against χ_c, we applied the same color-coding and shape-coding as described previously.

in the overlaid FT-IR spectra of the AS samples (Fig. 4a). The absorbance values for all other samples (AS, AN, AS-P, and AN-P) are provided in Table S4 and the corresponding spectra are reported in Fig. S4. Using Eq. (3), [71,72] we calculated the ferroelectric to paraelectric phase ratio (β/α). As expected, all samples exhibit high ferroelectric phase content, exceeding 90 % (Fig. 3b), as PVDF-TrFE copolymers preferentially crystallize in the β-phase. Notably, both the annealing and poling improve the ferroelectric phase content in all copolymers.

To better understand the interconnection between the various properties highlighted so far, we generated a correlation plot (Fig. 5). This was constructed by plotting the Pearson's correlation coefficients (*red squares* for positive coefficients, *blue* for negative ones) calculated for all variable pairs in the input matrix. Non-significant correlations (at a 95 % confidence level) are represented by empty squares. The matrix was assembled by combining data from DSC (Table S2), WAXD (Table S3), and FT-IR (Table S4). Descriptors were grouped by the technique used and, in the case of FT-IR data, based on peak assignments reported in the literature. The results show that parameters describing crystallinity, such as crystalline fraction (χ_c), crystallite size (D), Curie temperature (T_C), and Curie enthalpy (ΔH_C), are positively correlated with one another. These parameters also positively correlate with peaks typically assigned to the β-phase (1284 and 841 cm^{-1}) and, consequently, with the β/α phase ratio. Conversely, crystallinity-related parameters are negatively correlated with peaks associated with gauche defects (absorbances at 1238 and 906 cm^{-1}) as previously reported by Barique and Ohigashi [46], as well as with peaks corresponding to the α-phase (974, 808, and 760 cm^{-1}). A negative correlation with the TrFE content in the copolymer is also observed. Examining the descriptors for gauche defects reveals positive correlations with α-phase descriptors and TrFE content. As expected, given the negative correlations between α and β phases, the gauche defects show a negative correlation with the β-phase. For peaks at 1399 and 883 cm^{-1}, previously attributed by Arrigoni et al. to contributions from both crystalline phases [60], our correlation map indicates a significant affinity for the β-phase. However, important correlations are lost, such as the positive correlation with the β/α ratio and the negative correlation with the peaks attributed to the α-phase. Interestingly, the peak at 1083 cm^{-1}, which some authors attribute to the β-phase [60,65], behaves like an α-phase peak in our

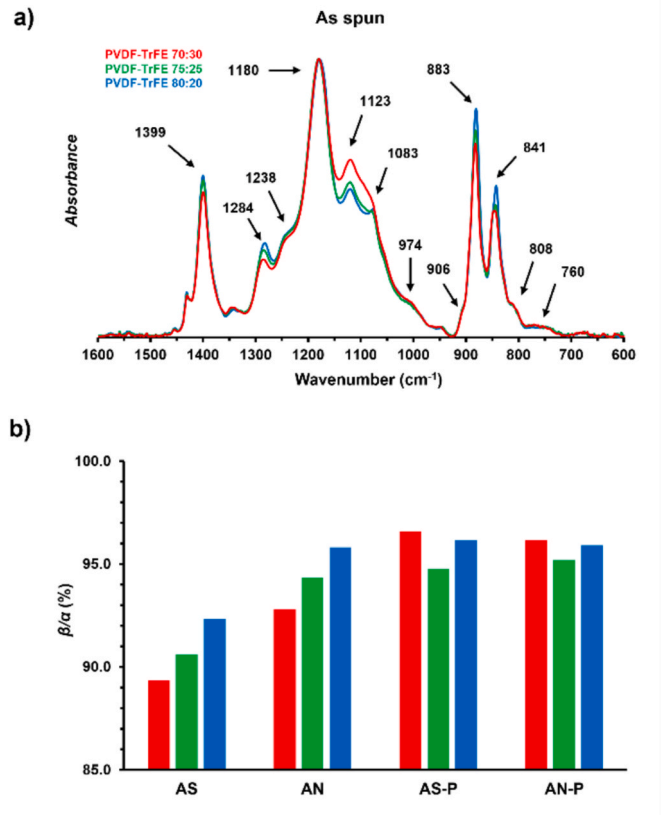

Fig. 4. a) Overlay of the normalized FT-IR spectra of the as-spun samples of the 70:30 (*red*), 75:25 (*green*), and 80:20 (*blue*) copolymers. We highlighted the peaks that were selected for a systematic comparison, as discussed in the manuscript. b) ferroelectric to paraelectric phase ratio (β/α) determined with Eq. (3) from FT-IR data.

correlation analysis. This is evidenced by its negative correlation with the β/α ratio and positive correlations with gauche defect descriptors.

Finally, we address the piezoelectric coefficient (d_{33}). The complete dataset of d_{33} values collected can be found in Table S5. Due to the intrinsic difference between the two sides of the sample (one yielding negative d_{33} values and the other positive) we reported the values of both sides, although we employed the mean absolute value in the following discussion. This choice is supported by a paired two-tailed *t*-test, which indicates no significant difference between the two distributions at 95 % confidence ($p = 0.061$). This parameter was not included in the correlation plot for two reasons: we obtained non-zero d_{33} values only for the polarized samples, and the 80:20 sample posed challenges. Fig. 3 shows that the 20-AN-P sample, after annealing and poling at 133 °C, has a T_C of 140 °C and a low d_{33} value of 13.5 ± 0.4 pC N^{-1} (Fig. 6A). With the intent to improve its piezoelectric charge coefficient, this sample was subjected to a second poling process at 140 °C, after which the d_{33} value increased to 26 pC N^{-1}, albeit being lower compared to the corresponding 20-AS-P sample having a d_{33} of 34.3 ± 0.6 pC N^{-1}. Furthermore, the poling at 140 °C, close to the T_m, caused partial melting of the sample leading to porosity loss (Fig. S5). Due to these considerations, data from the sample 20-AN-P were excluded from the following discussion regarding the influences of annealing and poling on the d_{33}. For the 70:30 and 75:25 copolymers, annealing improved the d_{33} values from 33 ± 2 pC N^{-1} to 36.9 ± 0.3 pC N^{-1} and from 35 ± 2 pC N^{-1} to 41 ± 2 pC N^{-1}, respectively. Fig. 6B, C, and D show a strong correlation between d_{33} values and crystallinity parameters: d_{33} increases with higher χ_c and larger *D*. Conversely, d_{33} decreases with an increase in gauche defects, exemplified by the absorbance at 906 cm^{-1}. The correlation between d_{33} and a linear combination of these parameters is very strong, with an R^2 value of 0.98 (Eq. (4), Fig. 6E).

$$d_{33} = 1.1 \bullet 10^{-3} \bullet \frac{\chi_C \bullet D}{A_{906}} + 25.71 \quad (4)$$

The apparent discrepancy in the behaviour of the 80:20 sample can be rationalized as follows. Experimental results indicate that the 20-AS sample possesses a crystalline phase rich in imperfections, which

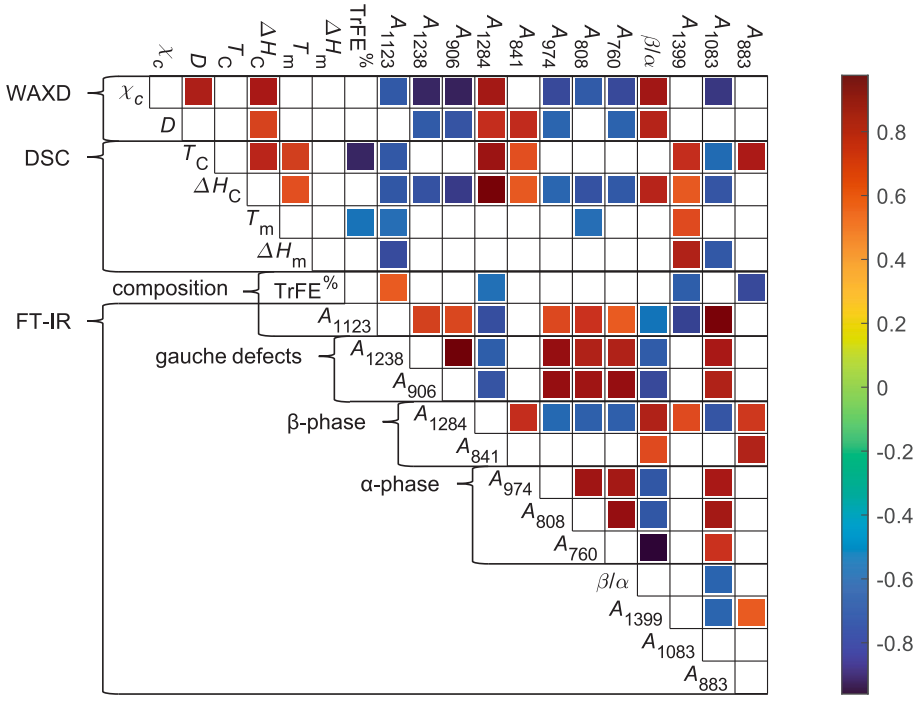

Fig. 5. Correlation plot of the descriptors defined for the twelve nanofibrous samples obtained through electrospinning and subsequent thermal and poling treatments. The color bar ranges from –1 (strong negative correlation, *blue*) to + 1 (strong positive correlation, *red*). Blank squares indicate non-significant correlations ($p > 0.05$). The variables are listed in the text.

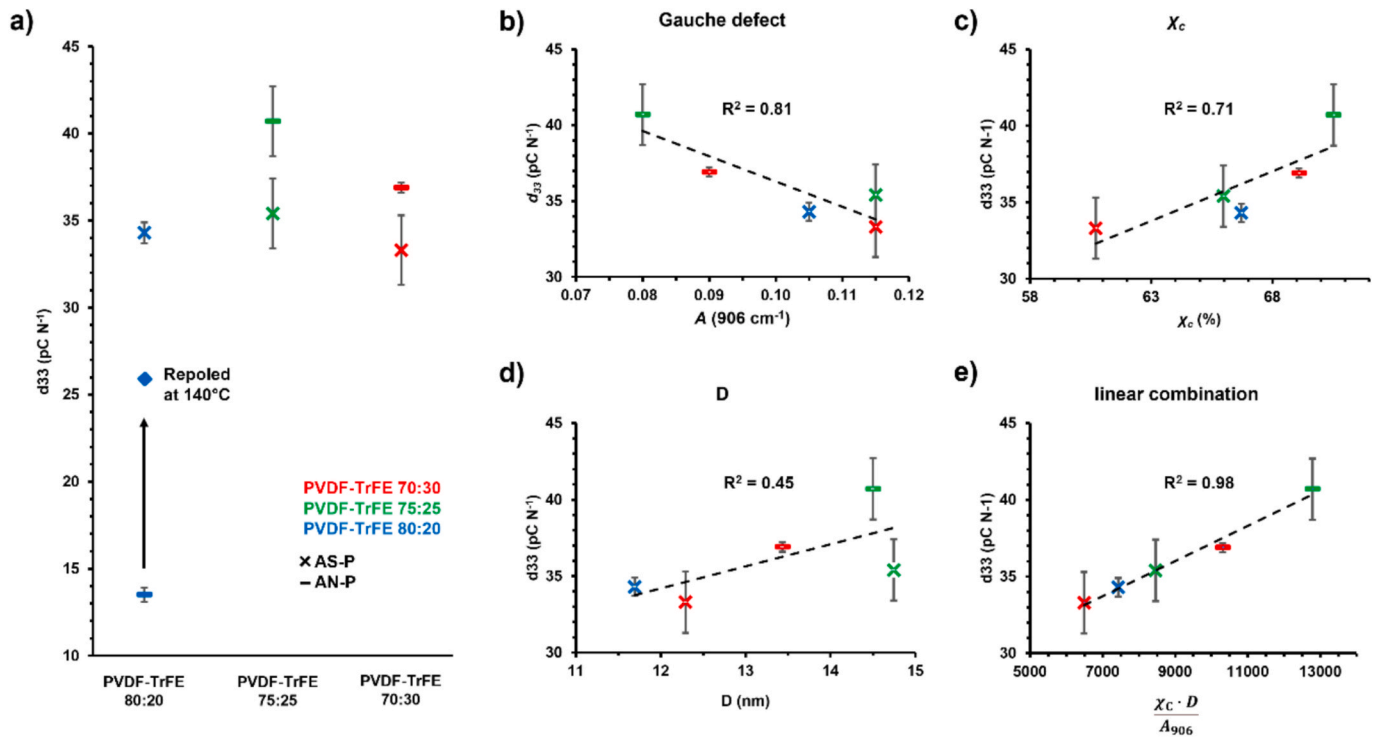

Fig. 6. a) Average values of d_{33} of the AS-P and AN-P samples. b) Plot of the d_{33} values as a function of the absorbance at 906 cm^{-1} (related to the gauche defects). c) Plot of the d_{33} values as a function of χ_c. d) Plot of the d_{33} values as a function of D. e) Plot of the d_{33} values as a function of the product between χ_c and D divided by the absorbance at 906 cm^{-1}. In b, c, d, and e plots, we excluded the d_{33} value of the 20-AN-P sample, and we also reported the trend line (*dashed black line*) with the corresponding regression coefficient.

renders the polymer chains highly susceptible to polarization when maintained at 133 °C, near the Curie temperature. At this temperature, the molecular chains exhibit enhanced mobility, facilitating their alignment under an applied electric field. Consequently, the 20-AS-P sample shows a significant increase in its piezoelectric coefficient, reaching a d_{33} value of 34.3 pC N^{-1}. In contrast, the 20-AN-P sample underwent substantial crystal quality improvement during the annealing process conducted in the absence of an electric field. This led to a notable reduction in the number of defects within its crystalline phase. The lower defect density hinders both the reorganization of the crystalline structure and the alignment of dipoles during the subsequent poling process, resulting in a lower d_{33} value (13.5 pC N^{-1}) compared to the 20-AS-P sample (34.3 pC N^{-1}). The attempt to repolarize the 80:20 sample at 140 °C led to an increase in d_{33} to 26 pC N^{-1}. Nevertheless, this value remains considerably lower than that of the 20-AS-P sample, supporting the hypothesis that improved crystalline quality limits the ability of the material to reorganize under an electric field, thereby reducing its overall polarizability. In contrast, the 75:25 and 70:30 copolymers, due to their higher TrFE content, exhibit a less compact crystalline structure than the 80:20 copolymer. This more open structure enhances polarizability, even after defect reduction via annealing. As a result, for copolymers with higher TrFE content, poling of annealed samples leads to a substantial increase in d_{33}.

Overall, the highest d_{33} values were found for the AN-P samples, being 42.7 pC N^{-1} measured for 75–25 copolymer and 36.9 pC N^{-1} for the 70–30 copolymer. To the best of our knowledge, these results represent the highest d_{33} values reported for nanofibrous PVDF-TrFE mats (Fig. 7 and Table S6), when considering only literature studies on electrospun fluoropolymer fibers in which the d_{33} values were measured using the same methodology employed in the present work (Berlincourt method), thereby enabling a consistent comparison.

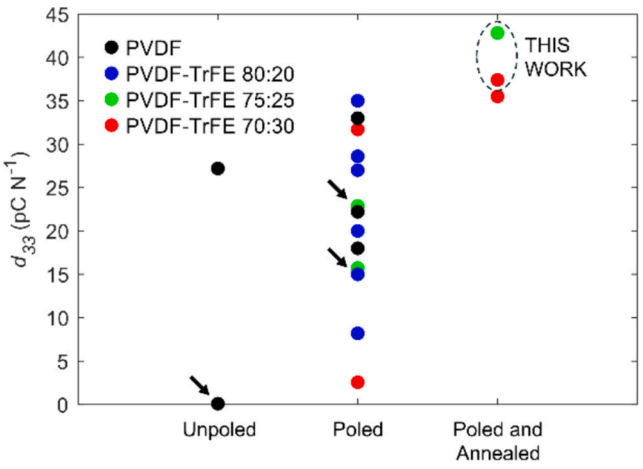

Fig. 7. Comparison between d_{33} absolute values reported in this work and other piezoelectric PVDF-based electrospun nanofibers, including PVDF, [45,73–76] PVDF-TrFE 80:20 [37,38,77–80], PVDF-TrFE 75:25 [81,82], and PVDF-TrFE 70:30 [83,84,85]. The arrow indicates samples for which the d_{31} piezoelectric coefficient was reported, rather than d_{33}.

3. Conclusion

This study investigated the influence of annealing and polarization on the structure and piezoelectric properties of PVDF-TrFE nanofibrous mats (70:30, 75:25, 80:20 molar fractions). Characterization techniques including SEM, DSC, WAXD, FT-IR, and piezometry were employed to correlate various structural and morphological parameters with piezoelectric properties. Results indicated no significant morphological differences between as-spun and annealed samples or across different molar fractions. However, poling led to the collapse of the morphology

on the side of the mat connected to the generator, unless preceded by annealing. The crystalline phase was characterized using WAXD data which highlighted that annealing strongly improved the crystallinity degree (χ_c), while poling significantly increased the crystallite size (D). Therefore, combined annealing and poling yielded the highest values for these parameters. As previously reported, FT-IR analysis revealed that annealing promoted the disappearance of gauche defects (1238 and 906 cm^{-1}). Herein we found how these positively correlate with α-phase peaks (808 and 760 cm^{-1}) but negatively correlated with β-phase peaks (1284 and 841 cm^{-1}). Gauche defects were also found to correlate negatively with χ_c and Curie enthalpy (ΔH_C). The piezoelectric coefficient (d_{33}) exhibited a positive correlation with χ_c and D but a negative correlation with FT-IR absorbances associated with gauche defects. Therefore, the synergic effect of annealing and poling treatment allowed to obtain some of the highest values of d_{33} ever reported in the literature for electrospun materials.

4. Experimental section

4.1. Materials

PVDF-TrFE copolymers with molar composition (VDF:TrFE) of 70:30 mol% (Solvene® 300), 75:25 mol% (Solvene® 250), and 80:20 mol% (Solvene® 200) were kindly provided by Solvay Specialty Polymers. Dimethylformamide (DMF, Sigma-Aldrich, ACS reagent, ≥99.8 %) and acetone (Ac, Sigma-Aldrich, ACS reagent, ≥99.5 %) were used without any further purification. The dielectric ester oil FR3 was supplied by CARGIL and was used after drying in a vacuum oven at 110 °C for 3 h.

4.2. Preparation of PVDF-TrFE electrospun mats

4.2.1. Electrospinning

PVDF-TrFE copolymers were dissolved in a 60:40 v/v Ac:DMF solution at a concentration of 19 % w/v in the case of 70:30 and 75:25 copolymers, and at 16 % w/v for the 80:20 copolymer. The solutions were stirred for 2 h at room temperature (RT) before being electrospun by using a home-made electrospinning apparatus composed of a SL 50 P10/CE/230 high-voltage power supplier (Spellman, New York, USA), a KDS-200 syringe pump (KDScientific Inc., Massachusetts, USA), a glass syringe containing the polymer solution, a stainless-steel needle (with an inner diameter of 0.5 mm) connected with the power supply electrode set at 22 kV, and a grounded plate collector positioned at a distance of 25 cm from the needle. The polymer solution was dispensed at the rate of 1.08 mL h^{-1}. The resulting mats (which ranged in thickness between 0.03 and 0.1 mm) were labelled as X-AS, where X indicates the molar content of TrFE units and AS stands for "As Spun".

Annealing treatment. Following established procedures [86,87], the AS samples were placed in a pre-heated oven for 24 h at their corresponding Curie Temperature. The latter was determined by Differential Scanning Calorimetry (DSC) from the second heating scan after controlled cooling at 10 °C min^{-1}. Specifically, annealing temperatures of 98 °C, 115 °C, and 133 °C were chosen for 30-AS, 25-AS, and 20-AS, respectively. The annealed samples were labelled as X-AN, where X indicates the molar content of TrFE units and AN stands for "Annealed".

4.2.2. Poling treatment

X-AS and X-AN samples were placed in the poling cell (Fig. S1) submerged in a temperature-controlled dielectric ester oil bath (FR3 natural ester, Cargil) as previously reported [38,77]. In a typical procedure, a 4 cm^2 sample was positioned between the high voltage electrode (1.8 cm^2) and a grounded electrode at a distance of 0.18 mm and gently immersed in the oil. The temperature program involved heating from room temperature (RT) to the previously defined Curie temperature, followed by a 30 min isothermal hold, and then cooling back to RT. After the first heating ramp, an electric field of 30 kV mm^{-1} was applied gradually using a Fug HCN 35 generator, and held constant for 30 min. Once at RT, the electric field was switched off. Afterwards, the mats were washed three times in cyclohexane to remove the oil. After drying, the edge of the sample that extend beyond the electrode (which served to prevent electrical breakdown) was cut away. Finally, both sides of the samples were grounded overnight to remove residual electrostatic charges. The poled samples were labelled either X-AS-P or X-AN-P, where X indicates the molar content of TrFE units, AS stands for "As Spun", AN stands for "Annealed" and P stands for "Poled". Additionally, the side of the mats adjacent to the high-voltage electrode was indicated as "live electrode side" (LES), while the one in contact with the grounded electrode was indicated as "grounded side" (GS).

4.3. Characterization methods

Scanning Electron Microscopy (SEM) observations were carried out using a Leica Cambridge Stereoscan 360 at an accelerating voltage of 20 kV. Morphological observations were performed on samples sputtered with gold. The distribution of fiber diameters was determined through the measurement of about 200 fibers and the results were reported as the average diameter (d) ± standard deviation (SD). The Student's t-test was used to verify the statistical significance of the difference between the mean values ($p < 0.05$). The collected data are reported in Table S1.

Differential Scanning Calorimetry (DSC) measurements were carried out using a TA Instruments Q2000 DSC, equipped with a Refrigerated Cooling System (RCS) system. To determine the annealing and poling temperatures, the samples were subjected to a first heating scan at 20 °C min^{-1} from −90 °C to 200 °C, a controlled cooling at 10 °C min^{-1} down to −90 °C and a second heating scan at 20 °C min^{-1}, in a nitrogen atmosphere. To measure the thermal properties of the nanofibrous mats, only the first heating scan was considered. The collected data are reported in Table S2.

Wide-Angle X-ray Diffraction (WAXD) was performed on a PANalytical X'Pert PRO diffractometer equipped with a fast solid state X'Celerator detector. CuKα radiation was used (40 mA, 40 kV). The 2θ range was from 10° to 50° with a step size of 0.033°, a time/step of 60 s, and a scan speed 0.07 ° s^{-1}. WAXD was used to determine the crystallinity and average domain size of the PVDF-TrFE mats. The diffractograms were analyzed with Fityk software to determine the relative area of the crystalline phase to the total area of the diffractogram. The crystalline fraction (χ_c) was calculated according to literature [63,88], using Eq. (1). Meanwhile, the average size of the crystalline domains (D) was calculated, according to literature [89], using the Scherrer Eq. (2). The collected data are reported in Table S3.

$$\chi_c(\%) = \frac{CrystllineArea}{CrystllineArea + AmorphousArea} \bullet 100 \quad (1)$$

$$D = \frac{k \bullet \lambda}{\beta \bullet \cos\theta} \quad (2)$$

where: k (the Scherrer constant) = 0.89, λ is the X-ray wavelength, β is the full width at half maximum (FWHM) of the diffraction peak, θ is the diffraction angle.

Fourier-transform infrared spectroscopy (FT-IR) spectra of the mats were collected on a Bruker model Alpha spectrophotometer equipped with ATR, in the 1600–600 cm^{-1} range with a resolution of 3 cm^{-1}. All spectra were normalized, according to literature [65], to the maximum peak at 1180 cm^{-1}. Following the literature [71,78], Eq. (3) was applied to determine the ratio of polar and non-polar polymorphs.

$$\beta/\alpha(\%) = \frac{A_{840}}{\frac{K_{840}}{K_{766}} \bullet A_{766} + A_{840}} \bullet 100 \quad (3)$$

where: $K_{840} = 7.7e+4$ and $K_{766} = 6.1e+4$, while A_{840} and A_{766} are the absorbances at 840 and 766 cm^{-1} after normalization, respectively. The collected data are reported in Table S4.

The piezoelectric effect was evaluated by measuring the piezoelectric d_{33} coefficient (pC N^{-1}), using high-precision piezometer (PiezoMeter System PM300, Piezotest, Singapore) by compressing the samples with an oscillating sinusoidal force of 0.25 N at 110 Hz with a grip force of 10 N. Three specimens for each type of sample were analysed by taking five measurements at both sides (the one in contact with the live electrode and the one in contact with the grounded electrode) and the d_{33} values were reported along with the corresponding standard deviation in Table S5.

4.4. Statistical analysis

The correlation plot was produced with MATLAB, namely using the *corrplot* function, by calculating the Pearson's correlation coefficients and setting a 95 % confidence level. The variables employed were: χ_c, D, T_C, the Curie enthalpy (ΔH_C), the melting temperature (T_m), the melting enthalpy (ΔH_m), $TrFE^{\%}$, β/α, and the FT-IR absorbances at: 1123, 1238, 906, 1284, 841, 974, 808, 760, 1399, 1083, 883 cm^{-1}.

CRediT authorship contribution statement

Michele Zanoni: Visualization, Investigation, Data curation, Writing – original draft, Methodology, Formal analysis, Conceptualization. **Niccolò Braidi:** Visualization, Data curation, Writing – review & editing, Formal analysis. **Giacomo Selleri:** Writing – original draft. **Dario Cavallo:** Writing – review & editing. **Maria Letizia Focarete:** Resources, Writing – review & editing. **Davide Fabiani:** Writing – review & editing, Resources, Supervision. **Chiara Gualandi:** Writing – review & editing, Resources, Funding acquisition, Supervision, Project administration, Conceptualization.

Declaration of competing interest

The authors declare the following financial interests/personal relationships which may be considered as potential competing interests: Gualandi Chiara reports financial support was provided by NATO. If there are other authors, they declare that they have no known competing financial interests or personal relationships that could have appeared to influence the work reported in this paper.

Acknowledgment

This work was supported by the North Atlantic Treaty Organization Science for Peace and Security Programme, grant project NATO SPS G5772.

Appendix A. Supplementary material

Supplementary data to this article can be found online at https://doi.org/10.1016/j.eurpolymj.2025.114159.

Data availability

Data will be made available on request.

References

[1] U. Pierre Claver, G. Zhao, Recent progress in flexible pressure sensors based electronic skin, Adv. Eng. Mater. 23 (5) (2021) 2001187, https://doi.org/10.1002/adem.202001187.
[2] W. Gao, H. Ota, D. Kiriya, K. Takei, A. Javey, Flexible electronics toward wearable sensing, Acc. Chem. Res. 52 (3) (2019) 523–533, https://doi.org/10.1021/acs.accounts.8b00500.
[3] H. Lim, H.S. Kim, R. Qazi, Y. Kwon, J. Jeong, W. Yeo, Advanced Soft materials, sensor integrations, and applications of wearable flexible hybrid electronics in healthcare, energy, and environment, Adv. Mater. 32 (15) (2020) 1901924, https://doi.org/10.1002/adma.201901924.
[4] Q. Shi, B. Dong, T. He, Z. Sun, J. Zhu, Z. Zhang, C. Lee, Progress in wearable electronics/photonics—moving toward the era of artificial intelligence and internet of things, InfoMat 2 (6) (2020) 1131–1162, https://doi.org/10.1002/inf2.12122.
[5] X. Pu, W. Hu, Z.L. Wang, Toward wearable self-charging power systems: the integration of energy-harvesting and storage devices, Small 14 (1) (2018) 1702817, https://doi.org/10.1002/smll.201702817.
[6] F. Mokhtari, G.M. Spinks, S. Sayyar, Z. Cheng, A. Ruhparwar, J. Foroughi, Highly stretchable self-powered wearable electrical energy generator and sensors, Adv. Mater. Technol. 6 (2) (2021) 2000841, https://doi.org/10.1002/admt.202000841.
[7] C. Xu, Y. Song, M. Han, H. Zhang, Portable and wearable self-powered systems based on emerging energy harvesting technology, Microsyst. Nanoeng. 7 (1) (2021) 25, https://doi.org/10.1038/s41378-021-00248-z.
[8] F.-R. Fan, Z.-Q. Tian, Z. Lin Wang, Flexible triboelectric generator, Nano Energy 1 (2) (2012) 328–334, https://doi.org/10.1016/j.nanoen.2012.01.004.
[9] C. Wu, A.C. Wang, W. Ding, H. Guo, Z.L. Wang, Triboelectric nanogenerator: a foundation of the energy for the new era, Adv. Energy Mater. 9 (1) (2019) 1802906, https://doi.org/10.1002/aenm.201802906.
[10] Y. Lee, J. Kim, B. Jang, S. Kim, B.K. Sharma, J.-H. Kim, J.-H. Ahn, Graphene-based stretchable/wearable self-powered touch sensor, Nano Energy 62 (2019) 259–267, https://doi.org/10.1016/j.nanoen.2019.05.039.
[11] Z.L. Wang, Triboelectric nanogenerators as new energy technology and self-powered sensors – principles problems and perspectives, Faraday Discuss 176 (2014) 447–458, https://doi.org/10.1039/C4FD00159A.
[12] G. Zhu, B. Peng, J. Chen, Q. Jing, Z. Lin Wang, Triboelectric nanogenerators as a new energy technology: from fundamentals, devices, to applications, Nano Energy 14 (2015) 126–138, https://doi.org/10.1016/j.nanoen.2014.11.050.
[13] W. Seung, M.K. Gupta, K.Y. Lee, K.-S. Shin, J.-H. Lee, T.Y. Kim, S. Kim, J. Lin, J. H. Kim, S.-W. Kim, Nanopatterned textile-based wearable triboelectric nanogenerator, ACS Nano 9 (4) (2015) 3501–3509, https://doi.org/10.1021/nn507221f.
[14] Y. Zhang, H. Kim, Q. Wang, W. Jo, A.I. Kingon, S.-H. Kim, C.K. Jeong, Progress in lead-free piezoelectric nanofiller materials and related composite nanogenerator, Devices. Nanosc. Adv. 2 (2020) 3131–3149, https://doi.org/10.1039/C9NA00809H.
[15] S. Maiti, S.K. Karan, J.K. Kim, B.B. Khatua, Nature driven bio-piezoelectric/triboelectric nanogenerator as next-generation green energy harvester for smart and pollution free society, Adv. En. Mat. 9 (9) (2019) 1803027, https://doi.org/10.1002/aenm.201803027.
[16] C. Lee, H. Park, J.-H. Lee, Recent structure development of poly(vinylidene fluoride)-based piezoelectric nanogenerator for self-powered sensor, Actuators 9 (2020) 57, https://doi.org/10.3390/act9030057.
[17] Y. Wu, Y. Ma, H. Zheng, S. Ramakrishna, Piezoelectric materials for flexible and wearable electronics: a review, Mater. Des. 211 (2021) 110164, https://doi.org/10.1016/j.matdes.2021.110164.
[18] C. Dagdeviren, P. Joe, O.L. Tuzman, K.-I. Park, K.J. Lee, Y. Shi, Y. Huang, J. A. Rogers, Recent progress in flexible and stretchable piezoelectric devices for mechanical energy harvesting, Sens. Actuat. Extreme Mech. Lett. 9 (2016) 269–281, https://doi.org/10.1016/j.eml.2016.05.015.
[19] Y. Meyer, R. Lachat, G. Akhras, A review of manufacturing techniques of smart composite structures with embedded bulk piezoelectric transducers, Smart Mater. Struct. 28 (5) (2019) 053001, https://doi.org/10.1088/1361-665X/ab0fab.
[20] N. Sezer, M. Koç, A comprehensive review on the state-of-the-art of piezoelectric energy harvesting, Nano Energy 80 (2021) 105567, https://doi.org/10.1016/j.nanoen.2020.105567.
[21] B. Singh, B. Padha, S. Verma, S. Satapathi, V. Gupta, S. Arya, Recent advances, challenges, and prospects of piezoelectric materials for self-charging supercapacitor, J. Energy Storage 47 (2022) 103547, https://doi.org/10.1016/j.est.2021.103547.
[22] J. Briscoe, S. Dunn, Piezoelectric nanogenerators – a review of nanostructured piezoelectric energy harvesters, Nano Energy 14 (2015) 15–29, https://doi.org/10.1016/j.nanoen.2014.11.059.
[23] X. Wan, H. Cong, G. Jiang, X. Liang, L. Liu, H. He, A review on PVDF nanofibers in textiles for flexible piezoelectric sensors, ACS Appl. Nano Mater. 6 (3) (2023) 1522–1540, https://doi.org/10.1021/acsanm.2c04916.
[24] F. Calavalle, M. Zaccaria, G. Selleri, T. Cramer, D. Fabiani, B. Fraboni, Piezoelectric and electrostatic properties of electrospun PVDF-TrFE nanofibers and their role in electromechanical transduction in nanogenerators and strain sensors, Macromol. Mater. Eng. 305 (7) (2020) 2000162, https://doi.org/10.1002/mame.202000162.
[25] J.S. Andrew, D.R. Clarke, enhanced ferroelectric phase content of polyvinylidene difluoride fibers with the addition of magnetic nanoparticles, Langmuir 24 (16) (2008) 8435–8438, https://doi.org/10.1021/la801617q.
[26] H. Gade, S. Nikam, G.G. Chase, D.H. Reneker, Effect of electrospinning conditions on β-phase and surface charge potential of PVDF fibers, Polymer 228 (2021) 123902, https://doi.org/10.1016/j.polymer.2021.123902.
[27] A. Baji, Y.-W. Mai, Q. Li, Y. Liu, Electrospinning induced ferroelectricity in poly (vinylidene fluoride) fibers, Nanoscale 3 (8) (2011) 3068, https://doi.org/10.1039/c1nr10467e.
[28] E.S. Cozza, O. Monticelli, E. Marsano, P. Cebe, On the electrospinning of PVDF: influence of the experimental conditions on the nanofiber properties, Polym. Int. 62 (1) (2013) 41–48, https://doi.org/10.1002/pi.4314.
[29] S.M. Damaraju, S. Wu, M. Jaffe, T.L. Arinzeh, Structural changes in PVDF fibers due to electrospinning and its effect on biological function, Biomed. Mater. 8 (4) (2013) 045007, https://doi.org/10.1088/1748-6041/8/4/045007.
[30] L. Persano, C. Dagdeviren, Y. Su, Y. Zhang, S. Girardo, D. Pisignano, Y. Huang, J. A. Rogers, High performance piezoelectric devices based on aligned arrays of

nanofibers of poly(vinylidenefluoride-co-trifluoroethylene), Nat. Commun. 4 (1) (2013) 1633, https://doi.org/10.1038/ncomms2639.
[31] H. Jiyong, Z. Yinda, Z. Hele, G. Yuanyuan, Y. Xudong, Mixed effect of main electrospinning parameters on the β -phase crystallinity of electrospun PVDF nanofibers, Smart Mater. Struct. 26 (8) (2017) 085019, https://doi.org/10.1088/1361-665X/aa7245.
[32] T. Yagi, M. Tatemoto, J. Sako, Transition behavior and dielectric properties in trifluoroethylene and vinylidene fluoride copolymers, Polym. J. 12 (4) (1980) 209–223, https://doi.org/10.1295/polymj.12.209.
[33] N. María, F. Le Goupil, D. Cavallo, J. Maiz, A.J. Müller, Effect of the TrFE content on the crystallization and SSA thermal fractionation of P(VDF-Co-TrFE) copolymers, Int. J. Mol. Sci. 23 (18) (2022) 10365, https://doi.org/10.3390/ijms231810365.
[34] H. Su, A. Strachan, W.A. Goddard, Density functional theory and molecular dynamics studies of the energetics and kinetics of electroactive polymers: PVDF and P(VDF-TrFE), Phys. Rev. B 70 (6) (2004) 064101, https://doi.org/10.1103/PhysRevB.70.064101.
[35] T. Soulestin, V. Ladmiral, F.D. Dos Santos, B. Améduri, Vinylidene fluoride- and trifluoroethylene-containing fluorinated electroactive copolymers. How does chemistry impact properties? Prog. Polym. Sci. 72 (2017) 16–60, https://doi.org/10.1016/j.progpolymsci.2017.04.004.
[36] X. Wang, F. Sun, G. Yin, Y. Wang, B. Liu, M. Dong, Tactile-sensing based on flexible PVDF nanofibers via electrospinning: a review, Sensors 18 (2) (2018) 330, https://doi.org/10.3390/s18020330.
[37] F. Mongiοì, G. Selleri, T. Maria Brugo, E. Maccaferri, D. Fabiani, A. Zucchelli, Multifunctional composite material based on piezoelectric nanofibers and Cu-CFRP electrodes for sensing applications, Compos. Struct. 337 (2024) 118076, https://doi.org/10.1016/j.compstruct.2024.118076.
[38] G. Selleri, M.E. Gino, T.M. Brugo, R. D'Anniballe, J. Tabucol, M.L. Focarete, R. Carloni, D. Fabiani, A. Zucchelli, Self-sensing composite material based on piezoelectric nanofibers, Mater. Des. 219 (2022) 110787, https://doi.org/10.1016/j.matdes.2022.110787.
[39] K. Krishnamoorthy, P. Pazhamalai, V.K. Mariappan, S.S. Nardekar, S. Sahoo, S.-J. Kim, Probing the energy conversion process in piezoelectric-driven electrochemical self-charging supercapacitor power cell using piezoelectrochemical spectroscopy, Nat. Commun. 11 (1) (2020) 2351, https://doi.org/10.1038/s41467-020-15808-6.
[40] F. Mokhtari, M. Shamshirsaz, M. Latifi, J. Foroughi, Nanofibers-based piezoelectric energy harvester for self-powered wearable technologies, Polymers 12 (11) (2020) 2697, https://doi.org/10.3390/polym12112697.
[41] S.S. Dani, B. Sundaray, S.K. Nayak, S. Mohanty, Electrospun PVDF and composite nanofiber: current status and future prescription towards hybrid piezoelectric nanogenerators, Mater. Today Commun. 38 (2024) 107661, https://doi.org/10.1016/j.mtcomm.2023.107661.
[42] D. Mandal, S. Yoon, K.J. Kim, Origin of piezoelectricity in an electrospun poly (vinylidene fluoride-trifluoroethylene) nanofiber web-based nanogenerator and nano-pressure sensor, Macromol. Rapid Commun. 32 (11) (2011) 831–837, https://doi.org/10.1002/marc.201100040.
[43] C. Chang, V.H. Tran, J. Wang, Y.-K. Fuh, L. Lin, Direct-write piezoelectric polymeric nanogenerator with high energy conversion efficiency, Nano Lett. 10 (2) (2010) 726–731, https://doi.org/10.1021/nl9040719.
[44] A. Forouzan, M. Yousefzadeh, M. Latifi, R. Jose, Effect of geometrical parameters on piezoresponse of nanofibrous wearable piezoelectric nanofabrics under low impact pressure, Macromol. Mater. Eng. 306 (1) (2021) 2000510, https://doi.org/10.1002/mame.202000510.
[45] S. Zhang, B. Zhang, J. Zhang, K. Ren, Enhanced piezoelectric performance of various electrospun PVDF nanofibers and related self-powered device applications, ACS Appl. Mater. Interf. 13 (27) (2021) 32242–32250, https://doi.org/10.1021/acsami.1c07995.
[46] M.A. Barique, H. Ohigashi, Annealing effects on the curie transition temperature and melting temperature of poly(vinylidene fluoride/trifluoroethylene) single crystalline films, Polymer 42 (11) (2001) 4981–4987, https://doi.org/10.1016/S0032-3861(00)00937-X.
[47] F. Bargain, P. Panine, F. Domingues Dos Santos, S. Tencé-Girault, From solvent-cast to annealed and poled poly(VDF-Co-TrFE) films: new insights on the defective ferroelectric phase, Polymer 105 (2016) 144–156, https://doi.org/10.1016/j.polymer.2016.10.010.
[48] H.J. Kantrow, C. Welton, N. Thomas, V. Sarou-Kanian, T. Pawlak, N. Stingelin, G.N. M. Reddy, A close look at the local structure of functional polymers: the example of poly(vinylidene fluoride), Adv. Funct. Mater. 2422354 (2025), https://doi.org/10.1002/adfm.202422354.
[49] Y. Guo, W. He, J. Liu, J. Wang, Charge characteristics of co-electrospun nanofiber membranes and their application in high-humidity environment, Separ. Purif. Tech. 359 (3) (2025) 130886, https://doi.org/10.1016/j.seppur.2024.130886.
[50] A. Enuka, M. Keblawi, E. Sedar, V. Beachley, A continuous manufacturing approach for aligned PVDF nanofiber yarns with enhanced mechanical and piezoelectric properties, ACS Appl. Polym. Mat. 7 (9) (2025) 5429–5436, https://doi.org/10.1021/acsapm.5c00069.
[51] M. Neidhöfer, F. Beaume, L. Ibos, A. Bernès, C. Lacabanne, Structural evolution of PVDF during storage or annealing, Polymer 45 (5) (2004) 1679–1688, https://doi.org/10.1016/j.polymer.2003.12.066.
[52] U. Montanari, D. Cocchi, T.M. Brugo, A. Pollicino, V. Taresco, M. Romero Fernandez, J.C. Moore, D. Sagnelli, F. Paradisi, A. Zucchelli, S.M. Howdle, C. Gualandi, Functionalisable epoxy-rich electrospun fibres based on renewable terpene for multi-purpose applications, Polymers 13 (11) (2021) 1804, https://doi.org/10.3390/polym13111804.
[53] M. Gazzano, C. Gualandi, A. Zucchelli, T. Sui, A.M. Korsunsky, C. Reinhard, M. L. Focarete, Structure-morphology correlation in electrospun fibers of semicrystalline polymers by simultaneous synchrotron SAXS-WAXD, Polymer 63 (2015) 154–163, https://doi.org/10.1016/j.polymer.2015.03.002.
[54] C. Gualandi, M. Govoni, L. Foroni, S. Valente, M. Bianchi, E. Giordano, G. Pasquinelli, F. Biscarini, M.L. Focarete, Ethanol disinfection affects physical properties and cell response of electrospun poly(l-lactic acid) scaffolds, Eur. Polym. J. 48 (12) (2012) 2008–2018, https://doi.org/10.1016/j.eurpolymj.2012.09.016.
[55] G. Teyssèdre, C. Lacabanne, Study of the thermal and dielectric behaviour of P (VDF-TrFE) copolymers in relation with their electroactive properties, Ferroelectrics 171 (1) (1995) 125–144, https://doi.org/10.1080/00150199508018427.
[56] K. Koga, H. Ohigashi, Piezoelectricity and related properties of vinylidene fluoride and trifluoroethylene copolymers, J. Appl. Phys. 59 (6) (1986) 2142–2150, https://doi.org/10.1063/1.336351.
[57] T. Yagi, Y. Higashihata, K. Fukuyama, J. Sako, Piezoelectric properties of rolled vinylidene fluoride and trifluoroethylene copolymer, Ferroelectrics 57 (1) (1984) 327–335, https://doi.org/10.1080/00150198408012771.
[58] J. Clements, G.R. Davies, I.M. Ward, A broad-line nuclear magnetic resonance study of a vinylidene fluoride/trifluoroethylene copolymer, Polymer 33 (8) (1992) 1623–1629, https://doi.org/10.1016/0032-3861(92)91058-A.
[59] Y. Liu, H. Aziguli, B. Zhang, W. Xu, W. Lu, J. Bernholc, Q. Wang, Ferroelectric polymers exhibiting behaviour reminiscent of a morphotropic phase boundary, Nature 562 (7725) (2018) 96–100, https://doi.org/10.1038/s41586-018-0550-z.
[60] A. Arrigoni, L. Brambilla, C. Bertarelli, G. Serra, M. Tommasini, C. Castiglioni, P (VDF-TrFE) nanofibers: structure of the ferroelectric and paraelectric phases through IR and raman spectroscopies, RSC Adv. 10 (62) (2020) 37779–37796, https://doi.org/10.1039/D0RA05478J.
[61] F. He, M. Sarkar, S. Lau, J. Fan, L.H. Chan, Preparation and characterization of porous poly(vinylidene fluoride-trifluoroethylene) copolymer membranes via electrospinning and further hot pressing, Polym. Test. 30 (4) (2011) 436–441, https://doi.org/10.1016/j.polymertesting.2011.03.005.
[62] H.-J. Chen, S. Han, C. Liu, Z. Luo, H.-P.-D. Shieh, R.-S. Hsiao, B.-R. Yang, Investigation of PVDF-TrFE composite with nanofillers for sensitivity improvement, Sens. Actuat. Phys. 245 (2016) 135–139, https://doi.org/10.1016/j.sna.2016.04.056.
[63] R. Sahoo, S. Mishra, L. Unnikrishnan, S. Mohanty, S. Mahapatra, S.K. Nayak, S. Anwar, A. Ramadoss, Enhanced dielectric and piezoelectric properties of Fe-doped ZnO/PVDF-TrFE composite films, Mater. Sci. Semicond. Process. 117 (2020) 105173, https://doi.org/10.1016/j.mssp.2020.105173.
[64] S. You, L. Zhang, J. Gui, H. Cui, S. Guo, A flexible piezoelectric nanogenerator based on aligned P(VDF-TrFE) nanofibers, Micromachines 10 (5) (2019) 302, https://doi.org/10.3390/mi10050302.
[65] B.M. Li, B. Ju, Y. Zhou, C.G. Knowles, Z. Rosenberg, T.J. Flewwellin, F. Kose, J. S. Jur, Airbrushed PVDF–TrFE fibrous sensors for E-textiles, ACS Appl. Electron. Mater. 3 (12) (2021) 5307–5326, https://doi.org/10.1021/acsaelm.1c00802.
[66] X. Liu, J. Tong, J. Wang, S. Lu, D. Yang, H. Li, C. Liu, Y. Song, BaTiO 3 /MXene/PVDF-TrFE composite films via an electrospinning method for flexible piezoelectric pressure sensors, J. Mater. Chem. C 11 (14) (2023) 4614–4622, https://doi.org/10.1039/D2TC05291A.
[67] Yi Xin, Tianyuan Hou, Chenyang Liu, Hongyan Liu, J. Tong, Yongchao Li, Tingting Lin, Flexible piezoelectric sensor based on PVDF-TrFE/nanoclay composite nanofibers for physiological micro-vibration signal sensing, Measurement 201 (2022) 111742, https://doi.org/10.1016/j.measurement.2022.111742.
[68] C.-Y. Tang, X. Zhao, J. Jia, S. Wang, X.-J. Zha, B. Yin, K. Ke, R.-Y. Bao, Z.-Y. Liu, Y. Wang, K. Zhang, M.-B. Yang, W. Yang, Low-entropy structured wearable film sensor with piezoresistive-piezoelectric hybrid effect for 3D mechanical signal screening, Nano Energy 90 (2021) 106603, https://doi.org/10.1016/j.nanoen.2021.106603.
[69] J. Li, C. Zhao, K. Xia, X. Liu, D. Li, J. Han, Enhanced piezoelectric output of the PVDF-TrFE/ZnO flexible piezoelectric nanogenerator by surface modification, Appl. Surf. Sci. 463 (2019) 626–634, https://doi.org/10.1016/j.apsusc.2018.08.266.
[70] R. Tanaka, K. Tashiro, M. Kobayashi, Annealing effect on the ferroelectric phase transition behavior and domain structure of vinylidene fluoride (VDF)–trifluoroethylene copolymers: a comparison between uniaxially oriented VDF 73 and 65% copolymers, Polymer 40 (13) (1999) 3855–3865, https://doi.org/10.1016/S0032-3861(98)00609-0.
[71] N. Meng, X. Zhu, R. Mao, M.J. Reece, E. Bilotti, Nanoscale interfacial electroactivity in PVDF/PVDF-TrFE blended films with enhanced dielectric and ferroelectric properties, J. Mater. Chem. C 5 (13) (2017) 3296–3305, https://doi.org/10.1039/C7TC00162B.
[72] L. Li, M. Zhang, M. Rong, W. Ruan, Studies on the transformation process of PVDF from α to β phase by stretching, RSC Adv. 4 (8) (2014) 3938–3943, https://doi.org/10.1039/C3RA45134H.
[73] A.H. Hassanin, E. Elnabawy, M. Salah, R. Nair, M. Gamal, N. Omran, A. Popelka, I. Kandas, N. Shehata, Multi-functional wet-electrospun piezoelectric nanofibers sensing mat: manufacturing, characterization, and applications, Mater. Sci. Semicond. Process. 166 (2023) 107708, https://doi.org/10.1016/j.mssp.2023.107708.
[74] L. Yang, M. Cheng, W. Lyu, M. Shen, J. Qiu, H. Ji, Q. Zhao, Tunable piezoelectric performance of flexible PVDF based nanocomposites from MWCNTs/Graphene/MnO_2 three-dimensional architectures under low poling electric fields, Compos. Part Appl. Sci. Manuf. 107 (2018) 536–544, https://doi.org/10.1016/j.compositesa.2018.02.004.

[75] F.-A. He, K. Lin, D.-L. Shi, H.-J. Wu, H.-K. Huang, J.-J. Chen, F. Chen, K.-H. Lam, Preparation of organosilicate/PVDF composites with enhanced piezoelectricity and pyroelectricity by stretching, Compos. Sci. Technol. 137 (2016) 138–147, https://doi.org/10.1016/j.compscitech.2016.10.031.

[76] M. Kubin, P. Makreski, M. Zanoni, L. Gasperini, G. Selleri, D. Fabiani, C. Gualandi, A. Bužarovska, Effects of nano-sized $BaTiO_3$ on microstructural, thermal, mechanical and piezoelectric behavior of electrospun PVDF/$BaTiO_3$ nanocomposite mats, Polym. Test. 126 (2023) 108158, https://doi.org/10.1016/j.polymertesting.2023.108158.

[77] G. Selleri, M.E. Gino, L. Gasperini, M. Zanoni, C. Gualandi, M.L. Focarete, D. Fabiani, Study on the polarization process for piezoelectric nanofibrous layers, in: 2021 IEEE Conference on Electrical Insulation and Dielectric Phenomena (CEIDP), IEEE, Vancouver, BC, Canada, 2021, pp. 61–64, https://doi.org/10.1109/CEIDP50766.2021.9705470.

[78] N. Hernández, V.A. González-González, I.B. Dzul-Bautista, N. Ornelas-Soto, J. M. Barandiarán, J. Gutierrez, Electrospun poly(vinylidene fluoride-trifluoroethylene) based flexible magnetoelectric nanofibers, Eur. Polym. J. 109 (2018) 336–340, https://doi.org/10.1016/j.eurpolymj.2018.09.045.

[79] G. Selleri, L. Gasperini, L. Piddiu, D. Fabiani, Comparison between AC and DC polarization methods of piezoelectric nanofibrous layers, in: 2022 IEEE 4th International Conference on Dielectrics (ICD), IEEE, Palermo, Italy, 2022, pp. 90–93, https://doi.org/10.1109/ICD53806.2022.9863546.

[80] G. Selleri, L. Gasperini, M. Zanoni, F. Depalma, C. Gualandi, D. Fabiani, Characterization of piezoelectric nanofibers for energy harvesting applications, in: 2022 IEEE Conference on Electrical Insulation and Dielectric Phenomena (CEIDP), IEEE:, Denver, CO, USA, 2022, pp. 270–273, https://doi.org/10.1109/CEIDP55452.2022.9985262.

[81] A. Wang, Z. Liu, M. Hu, C. Wang, X. Zhang, B. Shi, Y. Fan, Y. Cui, Z. Li, K. Ren, Piezoelectric nanofibrous scaffolds as in vivo energy harvesters for modifying fibroblast alignment and proliferation in wound healing, Nano Energy 43 (2018) 63–71, https://doi.org/10.1016/j.nanoen.2017.11.023.

[82] A. Wang, M. Hu, L. Zhou, X. Qiang, Self-powered well-aligned P(VDF-TrFE) piezoelectric nanofiber nanogenerator for modulating an exact electrical stimulation and enhancing the proliferation of preosteoblasts, Nanomaterials 9 (3) (2019) 349, https://doi.org/10.3390/nano9030349.

[83] M. Baniasadi, Z. Xu, S. Hong, M. Naraghi, M. Minary-Jolandan, Thermo-electromechanical behavior of piezoelectric nanofibers, ACS Appl. Mater. Interf. 8 (4) (2016) 2540–2551, https://doi.org/10.1021/acsami.5b10073.

[84] E. Stojchevska, P. Makreski, M. Zanoni, L. Gasperini, G. Selleri, D. Fabiani, C. Gualandi, A. Bužarovska, Piezoelectric PVDF-TrFE nanocomposite mats filled with $BaTiO_3$ nanofibers: the effect of poling conditions, Polym. Adv. Technol. 35 (2) (2024) e6333, https://doi.org/10.1002/pat.6333.

[85] J. Park, Y.-W. Lim, S.Y. Cho, M. Byun, K.-I. Park, H.E. Lee, S.D. Bu, K.-T. Lee, Q. Wang, C.K. Jeong, Ferroelectric polymer nanofibers reminiscent of morphotropic phase boundary behavior for improved piezoelectric energy harvesting, Small 18 (2022) 2104472, https://doi.org/10.1002/smll.202104472.

[86] C.Y.B. Ng, W.C. Gan, T.S. Velayutham, B.T. Goh, R. Hashim, Structural control of the dielectric, pyroelectric and ferroelectric properties of poly(vinylidene fluoride-co -trifluoroethylene) thin films, Phys. Chem. Chem. Phys. 22 (4) (2020) 2414–2423, https://doi.org/10.1039/C9CP01556F.

[87] R. Mahdi, W. Gan, W. Majid, Hot plate annealing at a low temperature of a thin ferroelectric P(VDF-TrFE) film with an improved crystalline structure for sensors and actuators, Sensors 14 (10) (2014) 19115–19127, https://doi.org/10.3390/s141019115.

[88] Y. Li, W. Feng, L. Meng, K.M. Tse, Z. Li, L. Huang, Z. Su, S. Guo, Investigation on in-situ sprayed, annealed and corona poled PVDF-TrFE coatings for guided wave-based structural health monitoring: from crystallization to piezoelectricity, Mater. Des. 199 (2021) 109415, https://doi.org/10.1016/j.matdes.2020.109415.

[89] F. Oliveira, Y. Leterrier, J. Månson, O. Sereda, A. Neels, A. Dommann, D. Damjanovic, Process influences on the structure, piezoelectric, and gas-barrier properties of PVDF-TrFE copolymer, J. Polym. Sci., Part B: Polym. Phys. 52 (7) (2014) 496–506, https://doi.org/10.1002/polb.23443.

Supporting Information

Optimizing the Piezoelectric Response of Poly(vinylidene fluoride-*co*-trifluoroethylene) electrospun mats: Effects of Copolymer Composition, Microstructure and Thermal Treatments

Michele Zanoni[a], *Niccolò Braidi*[a], *Giacomo Selleri*[b], *Dario Cavallo*[c], *Maria Letizia Focarete*[a,d,e], *Davide Fabiani*[b,f], *Chiara Gualandi*[a,d,f]*

[a] Department of Chemistry "Giacomo Ciamician", University of Bologna, Via Selmi 2, 40126 Bologna, Italy

[b] Department of Electrical, Electronic, and Information Engineering, University of Bologna, Viale Risorgimento 2, 40136 Bologna, Italy

[c] Department of Chemistry and Industrial Chemistry, University of Genova, Via Dodecaneso 31, 16146, Genova (Italy)

[d] INSTM UdR of Bologna, University of Bologna, Via Gobetti 85, 40129 Bologna, Italy

[e] Health Sciences & Technologies (HST) CIRI, University of Bologna, Via Tolara di Sopra 41/E, 40064 Ozzano Emilia Bologna, Italy

[f] Interdepartmental Center for Industrial Research on Advanced Applications in Mechanical Engineering and Materials Technology, CIRI-MAM, University of Bologna, Viale Risorgimento, 2, 40136 Bologna, Italy

E-mail: c.gualandi@unibo.it

Keywords: Electrospinning, piezoelectricity, PVDF-TrFE, Poling, Annealing

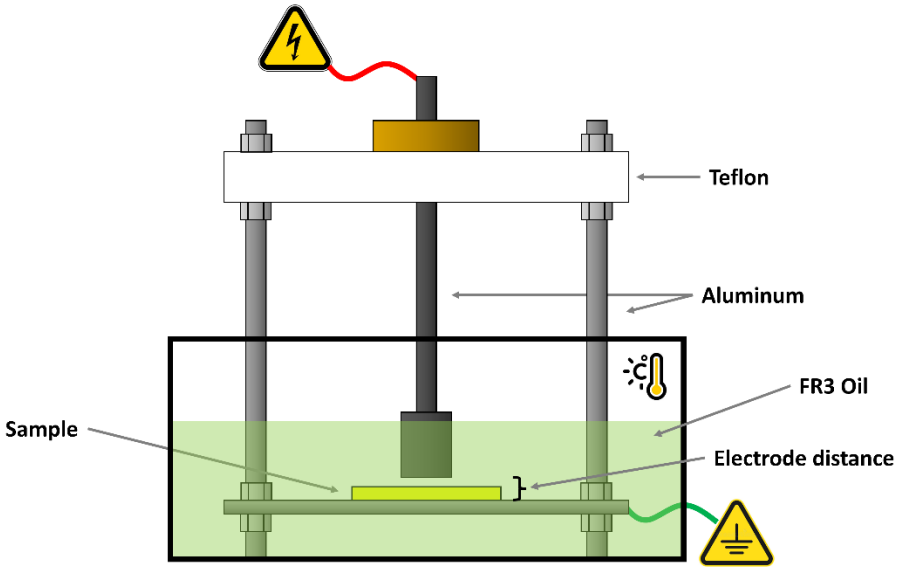

Figure S1. Scheme of the poling apparatus. The cell consists of a live electrode and a grounded electrode. The distance between electrodes was set at 0.18 mm since samples varied in thickness from 0.03 and 0.1 mm. This setup prevents the nanofibrous sample (in *yellow*) from being compressed by the electrode, thereby ensuring that the applied electric fields remain consistent. The cell is then immersed in the thermostated oil bath.

Table S1. Mean diameters (*d*) and corresponding standard deviations (*SD*) of the nanofibrous mats determined by scanning electron microscopy (SEM). LES = Live Electrode Side; GS = Grounded Side.

Sample	***d*** **[nm]**	***SD*** **[nm]**
30-AS	392	142
30-AN	384	138
30-AS-P (LES)	461	168
30-AS-P (GS)	460	159
30-AN-P (LES)	542	236
30-AN-P (GS)	468	244
25-AS	337	152
25-AN	304	91
25-AS-P (LES)	375	158
25-AS-P (GS)	337	99
25-AN-P (LES)	389	153
25-AN-P (GS)	338	114
20-AS	323	110
20-AN	320	124
20-AS-P (LES)	374	106
20-AS-P (GS)	378	111
20-AN-P (LES	399	139
20-AN-P (GS)	419	141

Table S2. Curie temperature (T_C) with its peak enthalpy (ΔH_C) and melting temperature (T_m) with its peak enthalpy (ΔH_m) determined from the second DSC heating scan.

Sample	T_C [°C]	ΔH_C [J g^{-1}]	T_m [°C]	ΔH_m [J g^{-1}]
30-AS	90	10	143	21
30-AN	97	24	145	28
30-AS-P	99	24	144	23
30-AN-P	103	23	143	24
25-AS	104	11	144	26
25-AN	116	32	146	31
25-AS-P	115	31	142	25
25-AN-P	121	33	145	29
20-AS	119	12	144	26
20-AN	134	38	149	31
20-AS-P	134	39	145	25
20-AN-P	140	44	150	26

Table S3. Crystallinity degree (χ_c) and crystallite size (D) of the nanofibrous mats determined by wide-angle X-ray diffraction (WAXD).

Sample	χ_c [%]	D [nm]
30-AS	43	8.4
30-AN	67	10.7
30-AS-P	61	12.3
30-AN-P	69	13.4
25-AS	50	9.6
25-AN	66	11.7
25-AS-P	66	14.7
25-AN-P	71	14.5
20-AS	54	9.4
20-AN	69	12.2
20-AS-P	67	11.7
20-AN-P	69	13.0

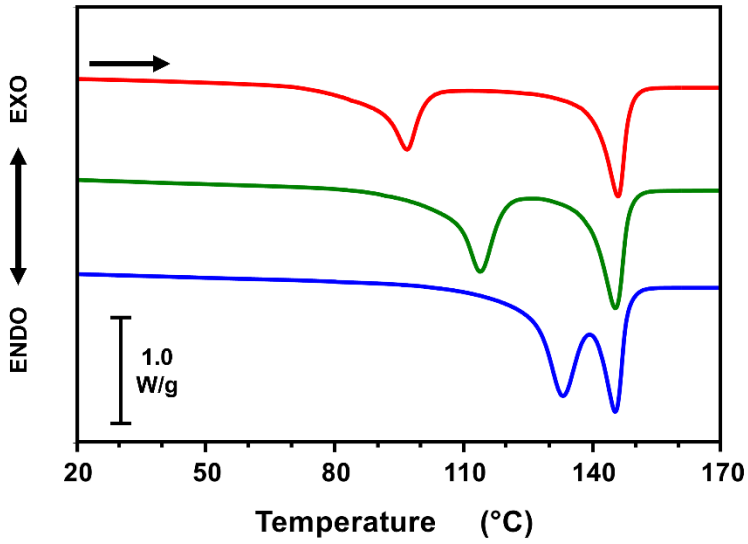

Figure S2. Second DSC heating scans performed after the complete melting and the controlled cooling at 10 °C min^{-1} on PVDF-TrFE 70:30 (red), PVDF-TrFE 75:25 (green), and PVDF-TrFE 80:20 (blue).

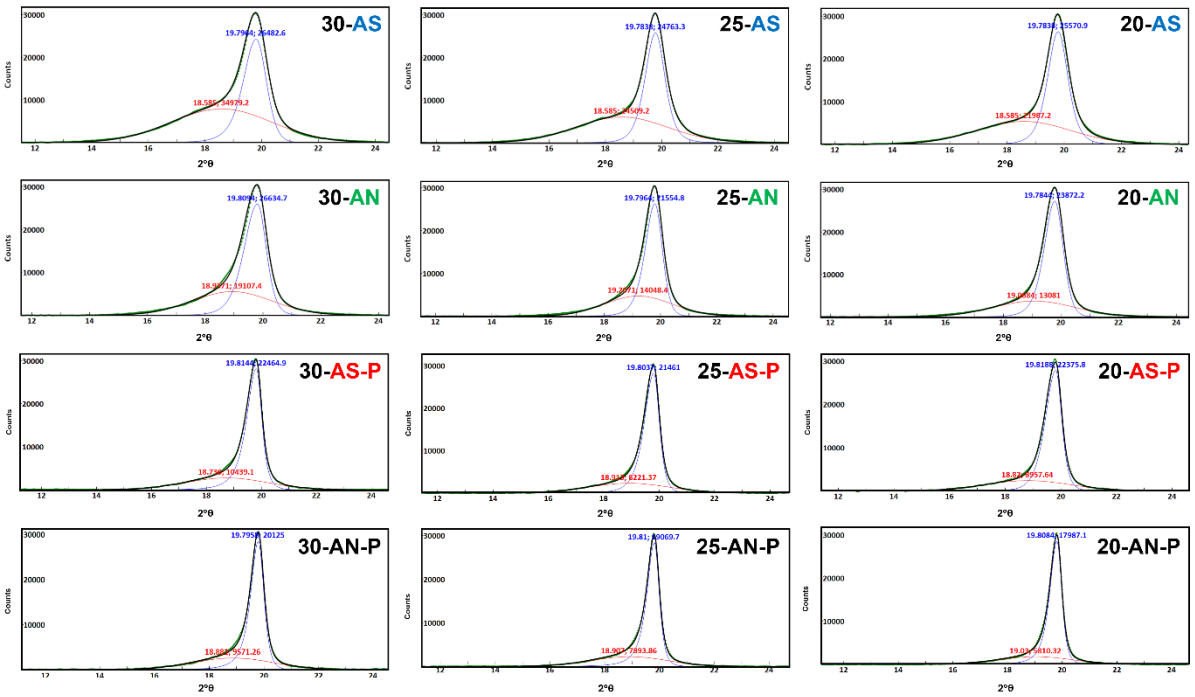

Figure S3: WAXD diffractograms of AS (first row), AN (second row), AS-P (third row), and AN-P (fourth row) samples for the three 70:30 (first column), 75:25 (second column), and 80:20 (third column) copolymers. The green dotted lines represent the original data. Red and blue curves are deconvoluted areas, representing the amorphous and crystalline phases, respectively. The black curve is the sum of the two. Note that the green and black lines are almost perfectly superimposed.

Table S4. Absorbances (A) of thirteen significant peaks in the range 1600 - 600 cm^{-1} determined by Fourier-transform infrared spectroscopy (FT-IR). LES = Live Electrode Side; GS = Grounded Side. The asterisked values were averaged between the LES and GS sides. For each peak, we tested for statistically significant differences between the values obtained from the LES and GS sides using a paired two-tailed t-test, which showed no significant difference between the two distributions at 95% confidence.

Sample	A_{1399}	A_{1284}	A_{1238}	A_{1123}	A_{1083}	A_{974}	A_{906}	A_{883}	A_{841}	A_{808}	A_{760}
30-AS	1.04	0.56	0.72	1.27	1.02	0.24	0.20	1.38	0.91	0.22	0.09
30-AN	1.10	0.68	0.62	1.01	0.77	0.16	0.12	1.35	0.88	0.18	0.06
30-AS-P (LES)	0.97	0.72	0.69	1.25	0.98	0.17	0.15	1.48	1.22	0.21	0.05
30-AS-P (GS)	1.14	0.70	0.63	1.05	0.80	0.14	0.08	1.32	0.88	0.12	0.01
30-AS-P*	1.05	0.71	0.66	1.14	0.88	0.15	0.10	1.40	1.02	0.15	0.02
30-AN-P (LES)	1.01	0.79	0.61	1.08	0.81	0.11	0.10	1.46	1.25	0.18	0.05
30-AN-P (GS)	1.05	0.67	0.59	0.99	0.72	0.06	0.08	1.35	0.90	0.13	0.02
30-AN-P*	1.03	0.73	0.60	1.04	0.77	0.09	0.09	1.41	1.08	0.16	0.04
25-AS	1.13	0.63	0.75	1.11	0.91	0.21	0.22	1.46	0.94	0.21	0.08
25-AN	1.32	0.79	0.61	0.85	0.69	0.13	0.09	1.44	0.92	0.14	0.04
25-AS-P (LES)	1.24	0.81	0.60	1.02	0.85	0.22	0.08	1.60	1.18	0.19	0.05
25-AS-P (GS)	1.05	0.82	0.69	1.10	0.89	0.18	0.15	1.68	1.36	0.23	0.06
25-AS-P*	1.15	0.82	0.65	1.06	0.87	0.20	0.12	1.64	1.27	0.21	0.06
25-AN-P (LES)	1.10	0.91	0.60	0.95	0.76	0.12	0.10	1.63	1.44	0.18	0.05
25-AN-P (GS)	1.25	0.78	0.57	0.87	0.69	0.06	0.06	1.53	1.05	0.15	0.05
25-AN-P*	1.18	0.85	0.59	0.91	0.73	0.09	0.08	1.58	1.25	0.17	0.05
20-AS	1.16	0.68	0.76	1.06	0.90	0.23	0.22	1.57	1.02	0.22	0.07
20-AN	1.35	0.86	0.59	0.79	0.69	0.13	0.09	1.63	1.11	0.14	0.04
20-AS-P (LES)	1.16	0.87	0.69	0.96	0.79	0.16	0.14	1.67	1.26	0.19	0.06
20-AS-P (GS)	1.33	0.86	0.58	0.78	0.65	0.10	0.07	1.58	1.09	0.09	0.02
20-AS-P*	1.25	0.87	0.64	0.87	0.72	0.13	0.11	1.63	1.18	0.14	0.04
20-AN-P (LES	1.22	0.89	0.60	0.89	0.72	0.12	0.07	1.60	1.23	0.13	0.03
20-AN-P (GS)	1.15	0.87	0.63	1.03	0.79	0.16	0.08	1.52	1.13	0.14	0.05
20-AN-P*	1.19	0.88	0.62	0.96	0.76	0.14	0.08	1.56	1.18	0.14	0.04

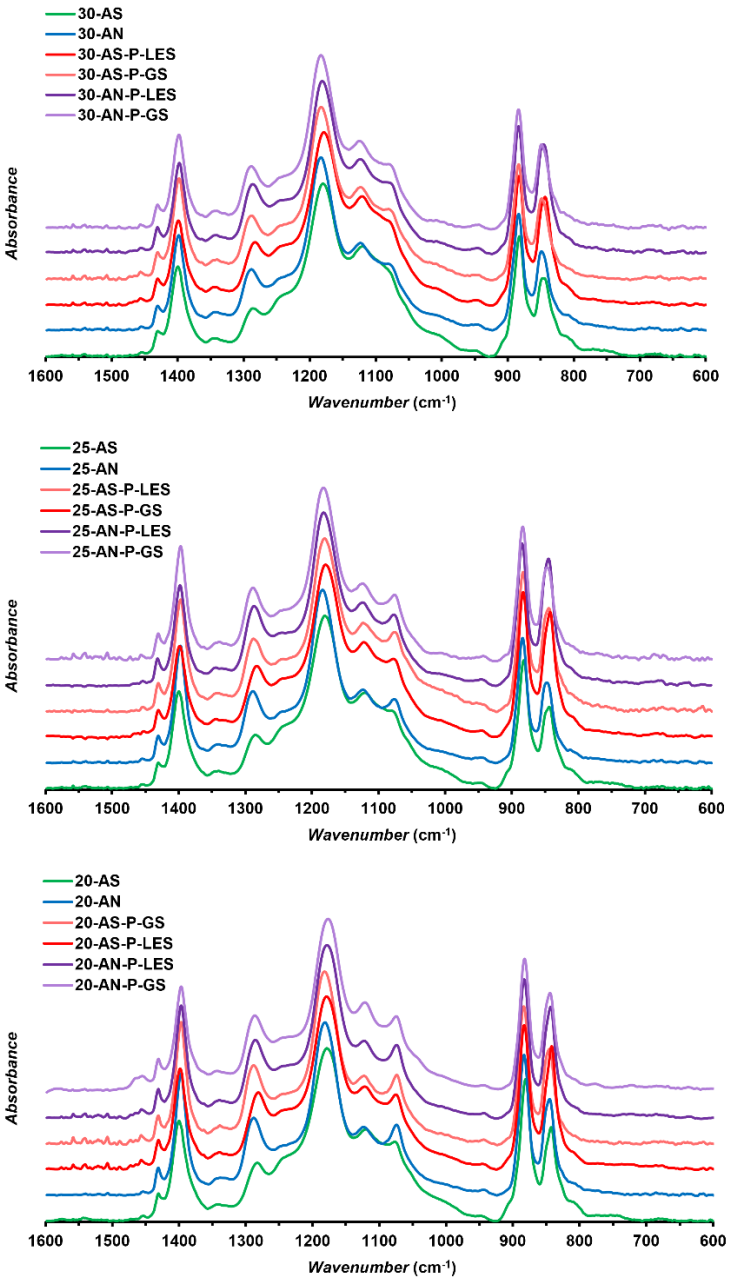

Figure S4: Overlay of FT-IR spectra. From top to bottom: overlays of AS, AN, AS-P, and AN-P samples (both LES and GS sides are shown for AS-P and AN-P) for the 70:30, 75:25, and 80:20 copolymers.

Table S5. Piezoelectric charge coefficients (d_{33}) measured for each type of sample on three specimens (named 1, 2, and 3) on both sides of the mat. The absolute mean values (mean d_{33}) and the corresponding standard deviations are also reported. LES = Live Electrode Side; GS = Grounded Side. We tested for statistically significant differences between the d_{33} values obtained from the LES and GS sides using a paired two-tailed t-test, which revealed no significant difference between the two distributions at 95% confidence.

Sample	***d*33 (LES) [pC N^{-1}]**	***d*33 (GS) [pC N^{-1}]**	***Mean d*33 [pC N^{-1}]**	***SD* [pC N^{-1}]**
30-AS	-0.13	-0.17	-0.15	0.08
30-AN	-0.12	-0.16	-0.14	0.12
25-AS	-0.16	-0.17	-0.17	0.14
25-AN	-0.15	-0.30	-0.22	0.17
20-AS	-0.09	-0.03	-0.06	0.04
20-AN	-0.08	-0.04	-0.06	0.06
30-AS-P (1)	-35.80	-34.00		
30-AS-P (2)	-32.22	-30.04	-33	2
30-AS-P (3)	-33.98	-33.80		
30-AN-P (1)	-37.14	-37.12		
30-AN-P (2)	-35.82	-37.24	-36.9	0.3
30-AN-P (3)	-36.64	-37.40		
25-AS-P (1)	-36.38	-36.48		
25-AS-P (2)	-37.40	-35.42	-35	2
25-AS-P (3)	-34.46	-32.00		
25-AN-P (1)	-42.62	-42.82		
25-AN-P (2)	-39.22	-38.64	-41	2
25-AN-P (3)	-41.02	-40.06		
20-AS-P (1)	-34.70	-34.44		
20-AS-P (2)	-34.70	-34.78	-34.3	0.6
20-AS-P (3)	-33.80	-33.30		
20-AN-P (1)	-13.64	-13.18		
20-AN-P (2)	-13.96	-13.88	-13.5	0.4
20-AN-P (3)	-13.16	-13.26		

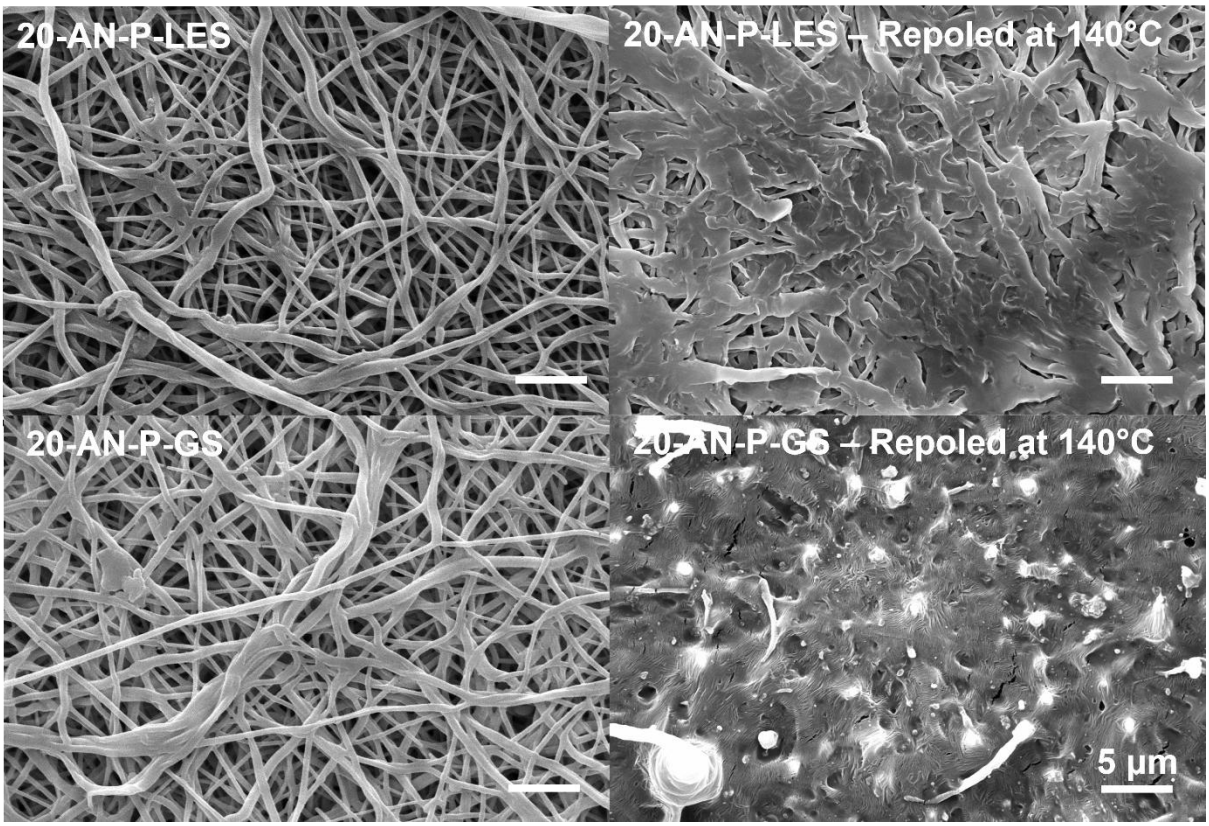

Figure S5: SEM micrographs of the 20-AN-P sample (LES and GS sides) before *(left column)* and after *(right column)* a second poling step at 140 °C.

Table S6. List of the scientific literature reporting piezoelectric coefficients, expressed in pC N^{-1}, measured on PVDF-based electrospun materials.

Sample	**Piezoelectric coefficient [pC N^{-1}]**	**Type of piezoelectric coefficient**	**Poling treatment**	**Reference number[a]**
PVDF	0.09	d_{31}	NO	45
PVDF	27.2	d_{33}	NO	73
PVDF + MnO_2/graphene/MWCNTs	33	d_{33}	YES	74
PVDF + organosilicate	22.2	d_{33}	YES	75
PVDF+ $BaTiO_3$	18	d_{33}	YES	76
PVDF-TrFE 80-20	8.2	d_{33}	YES	37
PVDF-TrFE 80-20	15	d_{33}	YES	77
PVDF-TrFE 80-20	28.6	d_{33}	YES	79
PVDF-TrFE 80-20	20	d_{33}	YES	80
PVDF-TrFE 80-20	27	d_{33}	YES	38
PVDF-TrFE 80-20 + $Nd_{0.05}Bi_{0.95}Fe_{0.95}Co_{0.05}O_3$	35	d_{33}	YES	78
PVDF-TrFE 75-25	15.73	d_{31}	YES	81
PVDF-TrFE 75-25	22.88	d_{31}	YES	72
PVDF-TrFE 70-30	35.5	d_{33}	YES	83
PVDF-TrFE 70-30	31.7	d_{33}	YES	84
PVDF-TrFE 70-30	2.56	d_{33}	YES	85

a) the indicated reference number is referred to the bibliographic list of the main manuscript.